72nd International Astronautical Congress, Dubai, United Arab Emirates, 25-29 October 2021.

IAC–21–66812

Multispectral Imaging Sensors for asteroids relative navigation

Margherita Piccinin,[*] **Gaia Letizia Civardi,**[†] **Matteo Quirino,**[‡] **and Michèle Lavagna**[§]

Abstract. Current missions to asteroids largely rely on visible imaging to perform relative navigation with respect to the target surface. A consequence of observing the body in the visible band is the large influence of illumination conditions, which could be mitigated by an imaging system working in other spectral bands. This paper studies the possibility to exploit multispectral imaging sensors for improving spacecrafts' relative navigation in proximity of asteroids. Realistic sensors models are considered and thermal images are synthetically generated exploiting physics-based models. An optical navigation algorithm for pose estimation is tested with visible and thermal images, proving the possible advantages of the multispectral strategy.

keywords: asteroids relative navigation, multispectral imaging, image-based navigation, microbolometers sensors, photon and thermal detectors, thermal imaging

1. Introduction

Spacecraft relative navigation techniques in proximity of asteroids largely rely on optical measurements taken from mono-cameras. In fact such sensors are passive and provide a wide operative range, generally required by the mission's operations. On the other hand, the visible imaging requires an adequate surface illumination to get fruitful measurements, posing several constraints to the spacecraft trajectories and operations.

Missions to celestial bodies typically carry other sensors on board, working in different spectral bands which could be exploited for navigation purposes. The Rosetta mission carried VIRTIS-M (Visible InfraRed and Thermal Imaging Spectrometer, Mapping channel), an hyperspectral imager performing 0.25–5.1 μm imaging spectroscopy on two separate channels [11]. The Hayabusa 2 mission to asteroid Ryugu, carried on board the TIR experiment, that collected far to close range thermal images of the surface in the Long Wave InfraRed spectrum, in the range 8-12 μm [20]. ESA's Hera mission payloads include both the AFC camera for navigation and imaging and the TIRI Thermal infrared imager (JAXA), which will be used for the observation of the asteroid night side [?].

This papers investigates the advantages of employing imaging systems working in different spectral bands for the purposes of on-board navigation in proximity of asteroids.

The use of multispectral imaging today is present in particular ground applications, such as detection and tracking of targets in the agricultural and military fields. The most common combination of cameras for multispectral imaging is thermal and visual [10]. Concerning relative navigation, thermal imaging is proposed as a method to overcome low-light conditions in visual odometry algorithms by means of non-uniformity correction techniques [5]. Multispectral Visual Odometry (VO) for unmanned air vehicles has been presented and experimentally validated [4]; while other works consider a multispectral SLAM (Simultaneous Localization And Mapping) approach for robot navigation [8, 16], also confirming experimentally [16] that the information added by the thermal camera improves the performance of the monocular SLAM approach (despite being used as independent, non-stereo sensors). Different techniques for exploiting the multispectral information exist, since the fusion can take place at different steps of the processing [15]. An option consists also in leaving the measurements as separated inputs for the navigation filter, depending on the application.

In the space field, thermal images have been exploited in the JAXA Hayabusa 2 mission for enhancing the detection of markers placed on the asteroid surface [19]. Such recent outcomes have highlighted the possibility to exploit sensors working in the infrared band for navigation purposes, along side with

---

[*] PhD Candidate, Politecnico di Milano, Italy, margherita.piccinin@polimi.it

[†] M.Sc. Student, Politecnico di Milano, Italy, gaialetizia.civardi@polimi.it

[‡] PhD Candidate, Politecnico di Milano, Italy, matteo.quirino@polimi.it

[§] Full Professor, Politecnico di Milano, Italy, michelle.lavagna@polimi.it

a more classical sensor suite. Possible useful applications include vision-based GNC algorithms for approaching a target body, operations in the night or in the dark area, but also moons and meteoroids detection, markers tracing, landing site selection and hazards detection.

This papers investigates the usefulness of employing a multispectral approach, exploiting images acquired in the visible and images in the thermal spectrum, for the purposes of on board GNC in proximity of an asteroid. An innovative navigation architecture which exploits both Visible (VIS) and Thermal Infrared (TIR) imaging is here presented. The paper major contributions are the following:

- to assess the feasibility of exploiting current imaging sensors technologies for the purpose of multispectral-based asteroid relative navigation;
- to determine the mission scenarios in which the multispectral approach produces the most significant improvements.

The paper is structured as follows. In Section 2, photon and thermal detectors working principles are introduced, presenting the models used for their suitability study. In Section 3, the scene-sensor chain architecture is presented, detailing the asteroids thermal modeling and the multi-spectral images generation process. Then, in Section 4 a multispectral navigation architecture for pose estimation in proximity of asteroids is proposed. Possible application scenarios are proposed in Section 5, with results shown and analysed in Section 6. The conclusions are finally presented in Section 7.

2. Sensors for multispectral imaging

In this section, the two major categories of sensors used in space for asteroids imaging in the visible and thermal spectral bands are presented.

In particular, Focal Plane Array (FPA) detectors are considered, being currently the dominant technology for cameras. Such sensors can be divided into two categories: photon detectors, that can work from the VIS to LWIR bands and thermal detectors, which work in the LWIR band, as shown in Fig. 1.

The main idea behind multispectral imaging consists in collecting images in specific and distinguished targeted spectral bands and exploit the differences among images to obtain the algorithms performance improvement.

- Thermal sensors typically present a smaller array size compared to photon sensors and for this reason they are less prone to navigation. The main disadvantage of using such sensors is their small array size, and thus the low resolution of available thermal images, which affects the performances of the image processing features extraction.
- Electro-optical sensors working in the visible band are largely affected by the illumination conditions [10]. Thermal sensors are less sensitive to illumination and can be employed also in the dark side if the body surface temperature is inside the instrument detection range.
- Thermal images have an advantage in optical navigation compared with optical images, since there are no other bright spots in the images such as background bright stars, bad pixels, or irradiation of solar wind particles or galactic rays, and there is no need to change the overexposure when the target is seen from a single pixel unit until a numerous pixel-sized body [19].

2.1 *Photon detectors*

Photon detectors convert the absorbed electromagnetic radiation directly into a change of the electronic energy distribution in a semi-conductor by the change of the free charge carrier concentration. The working principle of such materials consists in the generation of a photocurrent proportional to the intensity of the incident radiation. In particular, when the material is exposed to impinging photons, if their wavelength is inside the sensibility range of the material, electrons can be moved from their valence band to the conduction band, generating a current.

Sensor response Considering a point target in first approximation, the number of photons incident on the detector is computed as:

$$P_{px} = P_{sun}\left[\pi\frac{d^2}{2}\rho g(\phi)\right]\frac{1}{r^2}\left[\pi\frac{d_a^2}{4}\right]t_{exp} \qquad [1]$$

where P_{sun} the photon flux coming from the Sun at the target body, r is the range target-camera, ρ is the target reflectance, ϕ is the phase angle Sun-target-camera. The function $g(\phi)$ models the reflection on the target surface. The pixel response in DN is computed as:

$$r_{px} = \eta\frac{P_{px}}{G} \qquad [2]$$

where G is the camera gain and η is the detector efficiency, computed based on the fill factor FF,

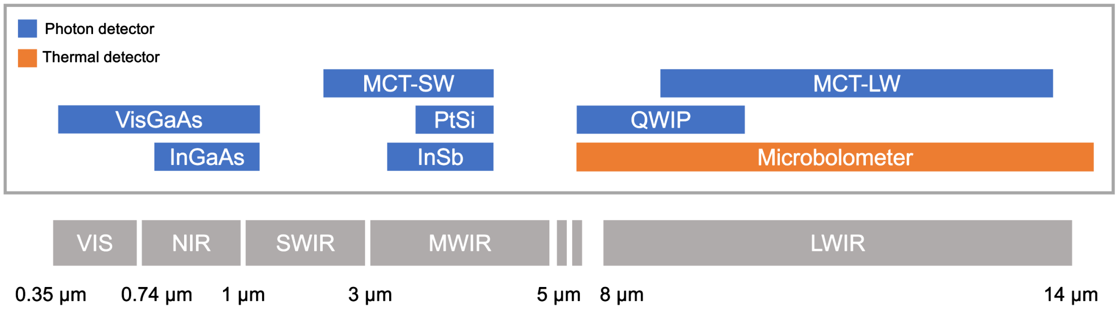

Fig. 1: Typical detector materials [2] operational range along the spectrum.

the detector quantum efficiency QE and the optical throughput η_{oe}:

$$\eta = \eta_{oe} \text{QE FF} \qquad [3]$$

Sensor noise Background noise (expressed in DN) is computed as the RMS of the noise sources: readout noise, dark current and shot noise [12] [9].

$$\begin{aligned} N &= \sqrt{\sigma_{shot}^2 + \sigma_{dark}^2 + \sigma_{read}^2} \\ &= \sqrt{N_{shot} + (N_{dark} t_{exp})^2 + N_{read}^2} \end{aligned} \qquad [4]$$

Shot noise is modeled as a Poisson process, hence its variance is equal to the mean: $N_{shot} = \eta P_{px}/G$.

2.2 *Thermal detectors*

Thermal detectors convert the absorbed electromagnetic radiation into thermal energy causing a rise in the detector temperature.

A common type of thermal detector is an uncooled microbolometer, made of a metal or semiconductor material. Microbolometer sensors present numerous advantages, such as the possibility to operate without cooling system; thus, having reduced dimensions, this technology is a promising option for deep-space cubesats as well, thanks to the small dimensions of such compact devices.

The working principle of a microbolometer consists in applying a bias voltage to a film of thermo-sensitive material through the readout circuit. If the thin film is irradiated by infrared radiation and heated, its resistance value is changed and the resistance changes is converted to a current or voltage signal that can be output by the readout circuit.

Sensor response The measurement provided by a microbolometer is proportional to the incoming scene radiation.

The pixel response r_{px} in $[DN]$ of the instrument can be modeled as:

$$r_{px} = G_{px} L + D_{px} \qquad [5]$$

where L is the scene radiance and G and D are parameters determined experimentally during the instrument characterization. In particular, G is the camera gain and D the camera offset, also known as dark signal. The parameters can be determined experimentally by imaging a black body that occupies the whole scene, at different temperatures. This procedure allows to retrieve the response of each pixel of the array as function of the scene radiance. Due to the non-uniformity of the detector, each pixel has a different response and thus the parameters G and D must be determined for each pixel *(i, j)*. Typically, the offset and sensitivity variations on the array are quite relevant, thus during operations dark frames are acquired to correct the response.

Scene radiance Ideally, the emitted scene radiance L can be computed by means of the Stephan-Boltzmann law as:

$$L_e = \epsilon \sigma T^{\alpha} \qquad [6]$$

where $\alpha = 4$. Whereas, the incoming radiance accounts for the view factor from the emitting body (i.e. the target asteroid) to the detector pixels:

$$L = F_{a-p} L_e \qquad [7]$$

The view factor F_{a-p} between the asteroid and pixel surfaces is:

$$F_{a-p} = \frac{1}{A_p} \int_{A_a} \int_{A_p} \frac{(\hat{\mathbf{n}}_a \cdot \mathbf{s}_{ap})(\hat{\mathbf{n}}_p \cdot \mathbf{s}_{pa})}{\pi S^4} dA_p dA_a \qquad [8]$$

where $\hat{\mathbf{n}}$ is the surface normal, $\mathbf{s}_{ij} = \mathbf{r}_j - \mathbf{r}_i$ is the position vector connecting the points on surface i with those on surface j and S is its magnitude $S = ||\mathbf{s}_{ji}|| = ||\mathbf{s}_{ij}||$.

Sensor responsivity The responsivity (or sensitivity) of a microbolometer array is defined as the ratio between the detector output voltage variation and the corresponding input temperature variation, expressed in $[DN/K]$. This corresponds to the slope of the response curve.

$$R(T) = \frac{dr_{px}(T)}{dT} \quad [9]$$

Using equations 5, 6 and 7 it turns to be:

$$R(T) = \alpha G_{px} F \epsilon \sigma T^{\alpha - 1} \quad [10]$$

From experiments, the sensitivity has been proved to be quite homogeneous on the detector, thus it can be approximated as independent from the (i, j) pixel [7].

Sensor noise Microbolometers sensors are characterized by the Noise Equivalent Temperature Difference (NETD), that is the minimum ΔT that the instrument can resolve. In particular, it corresponds to the T difference that a signal equal to the temporal noise (SNR = 1) would produce. It can be expressed as:

$$NETD = \frac{N_t}{R} \quad [11]$$

where N_t is the temporal noise ($[DN]$) and R the camera responsivity ($[DN/K]$).

Experimentally, the NETD can be determined as the difference in temperature between two side-by-side blackbodies which, when viewed by the camera, gives rise to a difference in SNR of 1 in the electrical output of the two halves of the array. It is important to highlight that the NETD depends on the instrument f-number, the exposure time and the operating temperature of the camera.

$$NETD = NETD(f_{num}, t_{exp}, T_{cam}) \quad [12]$$

3. Scene-image chain for thermal imaging

3.1 *Thermal images generation approach*

While traditional rendering techniques allow to generate visible synthetic images, analog tools for thermal images rendering do not exist. The architecture shown in Fig. 2 has been employed for realistic thermal images generation. From the asteroid and space environment inputs, a thermal simulation of the asteroid is performed, deriving the temperature distribution field at the trajectory epoch. An uncooled microbolometer sensor is modeled, accounting for the expected response from input radiation and the related NETD. A low-resolution temperature-image is used to mask a high-resolution rendered image of the asteroid surface. TIR images are processed to obtain a more representative appearance of the target asteroid. In particular, to match the expected microbolometer physical response - proportional to the radiation power absorbed by the detector pixels - masks are exploited.

3.2 *Asteroid thermal model*

The thermal model is exemplified in Fig 3, considering the contributions of the incoming Sun heat flux Q_{in}, the radiated flux Q_{out} and the heat transfer towards the ground layers Q_s:

$$Q_{in} = Q_{out} + Q_s \quad [13]$$

The solar flux depends on the distance between the Sun and the asteroid and on the incidence angle ϕ between the direction of the sun and the normal to the heated surface:

$$Q_{in} = S_{\odot}(1 - A)\left(\frac{AU}{r}\right)^2 \cos(\phi) \quad [14]$$

where $S_{\odot}$ is the solar constant, A is the bolometric Bond albedo and r is the distance to the Sun expressed in AU. The flux emitted from the asteroid at the thermal equilibrium is commonly written through the Stephan-Boltzmann law:

$$Q_{out} = \epsilon \sigma T^4 \quad [15]$$

where ϵ is the emissivity of the surface of the asteroid, σ is the Stefan-Boltzman constant and T is the temperature of the asteroid. The heat flux at the surface of the asteroid is linked to the the 1D temperature gradient

$$Q_s = -k \left.\frac{\partial T}{\partial x}\right|_{x=0} \quad [16]$$

being k is the conductivity of the ground of the asteroid. The x coordinate is taken in the radial direction, positive downwards. The heat conduction equation is then applied, in which a constant conductivity is assumed for simplicity:

$$\rho c_p \frac{\partial T(t,x)}{\partial t} = k \frac{\partial T(t,x)}{\partial x^2} \quad [17]$$

Finally, boundary conditions are set to complete the model:

$$\begin{cases} T(0,x) = f(x) & \forall\ x \in [0, l_s] \\ T_x(0,t) = \frac{Q_{out} - Q_{in}}{k} & \forall\ t \geq 0 \\ T_x(l_s,t) = 0 & \forall\ t \geq 0 \end{cases} \quad [18]$$

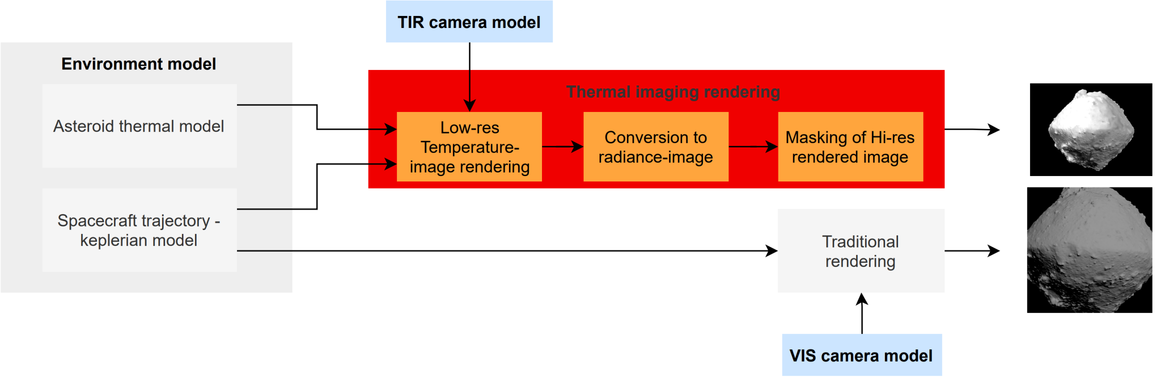

Fig. 2: Thermal images chain model.

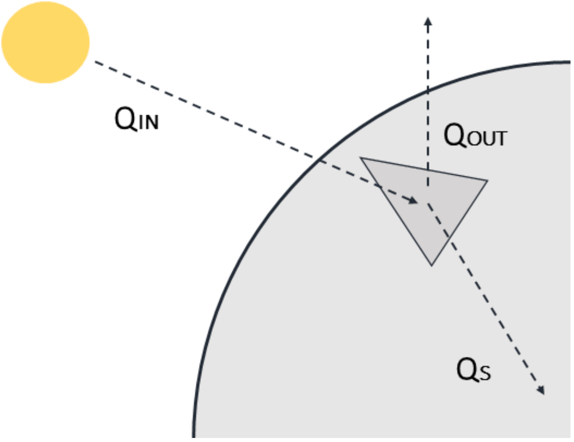

Fig. 3: Heat exchange model.

Where T_x denotes the partial derivative of temperature with respect to the spatial coordinate x and the skin depth l_s is regarded as the depth of the ground where an adiabatic assumption can be acceptable. A numerical finite-difference technique is used to solve the 1D heat conduction equation and an iterative technique is used to solve the surface boundary condition.

3.3 *Microbolometer response model*

Starting from the thermal sensor model presented in Section 2, the following assumptions are made. The responsivity is assumed homogeneous on the detector, therefore for a specific scene temperature $\bar{T}$:

$$R(\bar{T}) = \alpha(i,j)G(i,j)\bar{T}^{\alpha(i,j)-1} \qquad [19]$$

A mean value for α is taken, leaving the spatial dependence on the gain only [7]:

$$G = R(\bar{T})/(\alpha\bar{T}^{\alpha-1}) \qquad [20]$$

The non-uniformity of the detector gain and offset are accounted for, exploiting data available in the literature form experimental activities on space microbolometers sensors for asteroids thermal mapping [7]. Such effects are important to be modeled in case of the absence of non-uniformity corrections, which may be the case for on board application because of re-calibration needs or limited computational power reasons.

Thus the response is computed as:

$$r(T,i,j) = G(i,j)F\epsilon\sigma T^{\alpha} + D(i,j) + N_t \quad [DN] \qquad [21]$$

where $N_t = R(\bar{T})NETD$ and F is a simplified radiation view factor, for the case of emission from a sphere of radius R to small flat surface at distance H:

$$F = \left(\frac{R}{H}\right)^2 \qquad [22]$$

4. Navigation architecture

The vision-based navigation algorithm builds on concepts of Visual Odometry (VO) and Visual-SLAM (V-SLAM). Features are extracted and tracked from the incoming image stream, while at the same time a sparse 3D map of the asteroid is reconstructed and used for navigation. A schematic outline of the algorithm is presented in Fig. 4, while a brief summary is here presented.

Feature detection A *feature* or *keypoint* is defined as a point of interest in an image, usually in the form of corners, blobs and lines. Among all the different

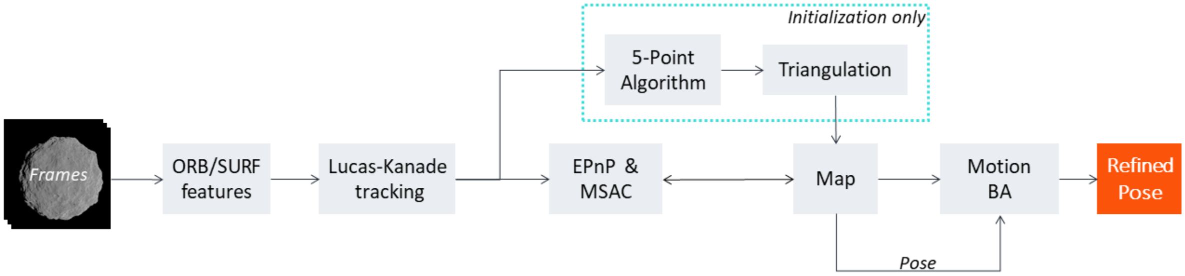

Fig. 4: Optical Navigation system overview.

feature extraction approaches, Oriented FAST and Rotated BRIEF (ORB) [21] is exploited due to its computational efficiency. To further improve the spatial keypoint distribution over the image, adaptive non-maximal suppression (ANMS) with suppression via square covering (SSC) is employed [3], that is able to enforce a better spatial distribution by jointly taking into account the keypoints strength and their localization. An upper bound of 400 features is then set to constrain the computational burden.

Feature tracking Features are extracted from the first frame and are then tracked on the subsequent images using the pyramidal Lucas-Kanade algorithm [6]. The number of tracked features tends to decrease as the trajectory develops, therefore new keypoints must be initialized. New features are merged with the old ones that are still being tracked at the time of re-detection, provided that they are sufficiently distant.

Motion Estimation In the main V-SLAM module, motion estimation relies on correspondences between 2D tracked features and 3D map points. For this reason, the map must be built and initialized to bootstrap the algorithm. In the initialization module, keypoints detected in the first frame are tracked from the first frame through all intermediate frames up to the actual second initialization frame. The essential matrix is estimated through the 5-point algorithm [18], that is nested within an MSAC [23] routine for robustness purposes. The essential matrix is then decomposed using Singular Value Decomposition (SVD), obtaining a rotation matrix and a translation vector (up to scale). Landmarks can be now triangulated using the relative pose information. Once the 3D sparse map is initialized and the 2D features are tracked, for each incoming image a set of 3D to 2D map to features correspondences is retrieved and used to solve the *Perspective-n-Point problem* (PnP). P3P [24] and EPnP [14] algorithms are exploited to this aim. The P3P algorithm is combined with MSAC in order to remove outliers from the initial set of correspondences. The resulting set of Map-To-Frame correspondences is then fed to the EPnP solver, that is a non-iterative solution of the problem and is applicable both for planar and non planar map point configurations. The last step is represented by a Gauss-Newton iterative optimization, which further refines the EPnP pose estimate.

Mapping When the map is first initialized, badly triangulated landmarks must be pruned to preserve localization performances. Landmarks must have a positive z coordinate in the current camera frame, which means that they are actually in front of the camera and visible. Furthermore, an upper limit on the distance from the camera is imposed, since far away points tend to have a higher uncertainty. Each time new keypoints are initialized, an attempt of triangulation is made, using the previously stored pose information. To make sure that the newly added landmarks respect some quality standards, the angle between the between the bearing vectors corresponding to the keypoints observations and camera poses must be greater than a predefined value. In addition, the reprojection error of the candidate landmarks must not exceed a defined error threshold.

Optimization Motion estimation is an error prone step and it does not have sufficient accuracy in trajectory reconstruction by itself. Besides, motion is reconstructed in an incremental way, which means that error tends to build up and exponentially grow as the trajectory develops. To prevent the motion estimation error from accumulating, Bundle Adjustment (BA), that is an optimization technique, is exploited. To reduce the computational load of the algorithm, Motion Only BA is performed, meaning that only the pose is optimized, keeping the 3D landmark coordinates fixed.

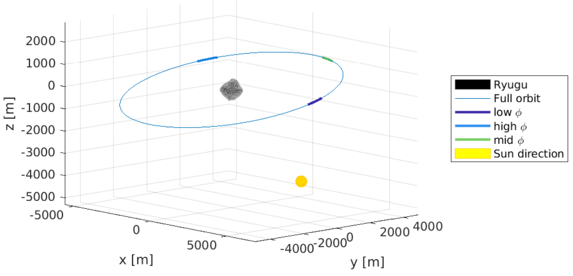

Fig. 5: Spacecraft inertial orbit with different illumination study cases.

5. Simulation scenarios

In this section, the selected simulation scenarios are presented.

5.1 *Orbital and mission scenario*

The scenario under study is the one of asteroid 162173 Ryugu, for which numerous recent mission data are available. The navigation architecture is tested considering a keplerian circular orbit at 5 km distance from Ryugu, with an inclination of 11°, shown in Fig. 5. Please note that Ryugu's mean diameter is 870 m.

Four case studies are analyzed. The considered cases differ only regarding the illumination conditions (phase angle ϕ) and asteroids thermal inertia Γ. Such parameters are in fact potential weaknesses of VIS-only and TIR-only navigation and thus a potential area of improvement with a multispectral approach. The actual Γ of Ryugu is employed in cases 1-3 and a different one is chosen for case 4.

1. **Low phase angle.** In this case the s/c is on the light side of the asteroid.

2. **Intermediate phase angle.** The s/c is looking at the terminator.

3. **High phase angle.** The s/c is on the eclipse side of the asteroid.

4. **High phase angle + high thermal inertia.** The s/c is on the eclipse side of the asteroid and a high thermal inertia is assumed for Ryugu.

Each arc has a duration of about 3 h and the considered sampling rate is 1 frame per minute, due to the slow relative dynamics.

5.2 *Sensors for multispectral imaging selection*

Given the orbital scenario presented in section 5.1, the grey-body emitted radiation (Planck's law) and the radiation reflected by the target at a 5 km distance is shown in Fig. 6. Reflectance and emissivity coefficients for Ryugu are $\rho = 0.02$ and $\epsilon = 0.9$ from the Hayabusa 2 mission data analyses [19] [13].

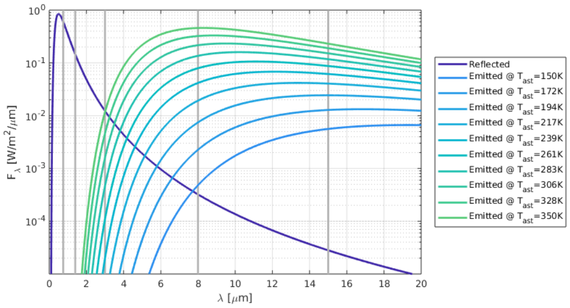

Fig. 6: Radiation emitted and reflected from Ryugu at 5 km.

The selected bands of interest for the multispectral imaging are consequently the VIS and LWIR band, being not overlapping and corresponding respectively to the peaks of reflection and emission. The main purpose of this paper is in fact to study the benefits of exploiting imaging coming from well separated bands and thus carrying different information.

The TIR and VIS cameras characteristics are reported in Table 1. In particular, for the TIR the real HW characteristics of Hayabusa 2 TIR payload have been considered, while for the VIS sensor common characteristics have been chosen, in order to have as expected a wider array size and a similar but smaller FoV (Field of View).

6. Results

The SLAM algorithm is tested on synthetic images: VIS images are generated by means of classical rendering techniques, while TIR images are obtained from the the asteroid surface thermal behaviour modeling. Results are discussed in this section, examining thermal simulation results, sensors response results and optical navigation performances.

Table 1: Cameras characteristics.

TIR	
array size	344 x 260
FoV	16.7° x 12.7°
NETD	0.4 K
bit depth	12
detectable temperature	150 - 460 K
spectral band	8 - 12 μm
VIS	
array size	1024 x 1024
FoV	10° x 10°
bit depth	8
spectral band	380-750 nm

6.1 *Thermal simulation results*

Ryugu's thermophysical properties used for the thermal analysis are reported in Table 2 [22]. The asteroid shape model used is available from Hayabusa 2 mission data [1].

Table 2: Ryugu's thermophysical properties.

Parameter	**Value**	**Unit**
Emissivity	0.9	-
Bond albedo	0.0146	-
Thermal inertia Γ	225	$Js^{1/2}K^{-1}m^{-2}$
Density	1192.8	kgm^{-3}
Heat capacity	600	JK^{-1}

For each case study, the minimum and maximum temperatures on the asteroid surface are approximately constant along the whole orbit, being in range $146 - 397$ K. Such results are in accordance with the actual Ryugu surface temperature, which is estimated to typically range from 250 to 400 K during daytime and down to 150 K during nighttime [20].

From the thermal simulations in cases 1-3, it has been observed that the low thermal inertia causes fast temperature changes on the surface as the asteroid rotates on its spin axis. This means that the phase angle is tightly related with the temperature field on the surface.

6.2 *Sensor response results*

Microbolometer response result Representative data for the sensor model have been taken from calibration experiments on microbolometer for asteroids observation [7]. In particular, the available non uniformity textures of responsivity and offset have been tailored on the present study case. The textures are resized with TIR array dimensions; while the offset and gain values are scaled according to the TIR bit depth and operative detection temperature range. The resulting detector response and offset values at the mean expected temperature are shown respectively in Fig. 8 and 9.

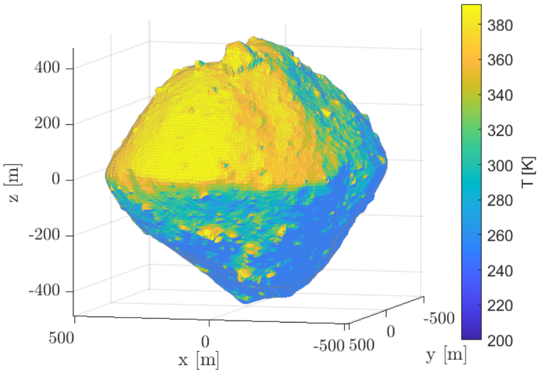

Fig. 7: Temperature field, high Sun phase angle.

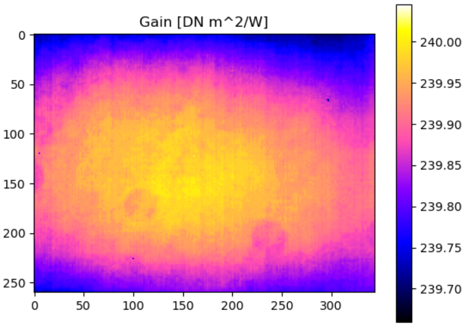

Fig. 8: Modeled detector gain for blackbody scene at $T_{mean} = 305$ K. Base texture from literature real sensor data [7].

An example of pixels' responses with large differences in offset and sensitivity is shown in Fig. 10 for the whole operative detection temperature range. As it can be noticed, the non-uniformity effects can be quite relevant. Thus, their modeling shall be included for realistic thermal images generation. In fact, for a real-time on board application, as the relative navigation treated here, corrections might not applied to images or they might degrade in time, becoming potentially dangerous to the navigation.

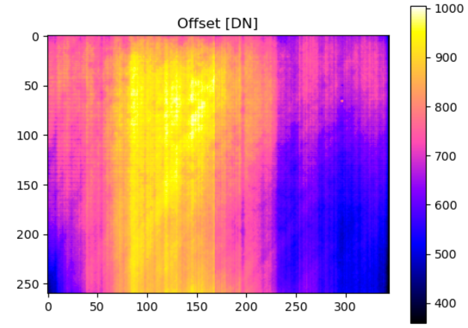

Fig. 9: Modeled detector offset for blackbody scene at $T_{mean} = 305$ K. Base texture from literature real sensor data [7].

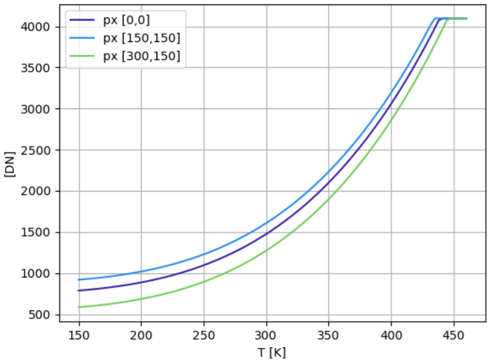

Fig. 10: Pixel response examples.

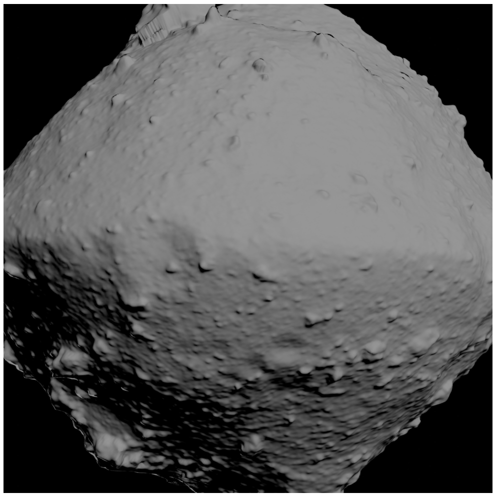

Fig. 11: Example of VIS camera image in the high phase angle case.

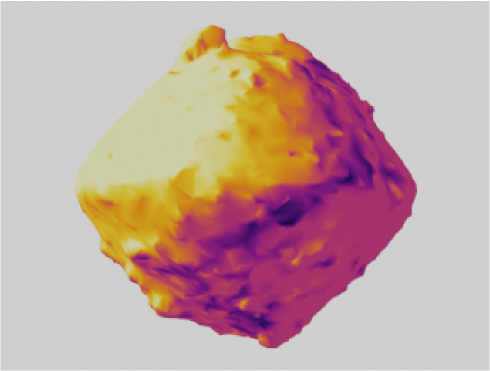

Fig. 12: Example of temperature intermediate image in the high phase angle case.

Generated images Examples of the generated temperature field, VIS and TIR images are shown respectively in Fig. 12, 11 and 13. What can be noticed is the large appearance difference between the VIS and TIR images, not only in relation to form factor and resolution, but also in the brightness distribution and presence of features on different surface areas. Possible improvements to the generation process are the inclusion of different emissivity values of the asteroids terrain and rocks and the computation of the asteroid-pixel view factor F_{a-p} from a shape model, instead of the spherical approximation.

In cases 1-3, due to the very low inertial of asteroid Ryugu, the phase angle has a relevant influence on the thermal images as well. As a consequence, in the low ϕ case, the TIR observes mainly the hottest regions of the surface; while in the high ϕ the coldest ones. Simulations have highlighted that due to Ryugu low thermal inertia, the thermal images in eclipse are quite dark. Being large areas of the body neither visible in the optical band, neither from the thermal camera, both bands result to be not useful for optical navigation in the high ϕ scenario. In fact, considering that the simulated temperatures are in range 146 to 397 K and that Hayabusa TIR covers temperatures in range $150 - 460K$, but can work properly only in the range 230 to 420 K [20], such result is in line with the mission data.

For this reason, the 4th study case is considered, which is identical to case 3, but consideres some fictitious physical properties, as a higher thermal inertia, which lead to hotter temperatures in shadow. In this case, VIS images have a bad quality, but the asteroid is observable with the TIR camera.

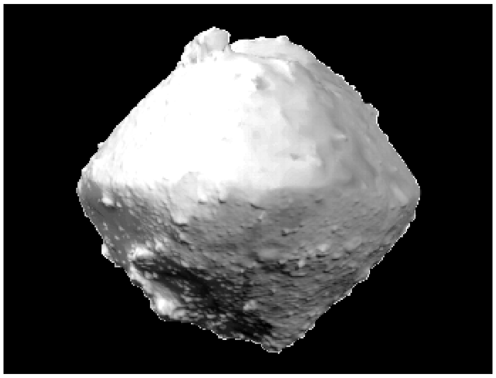

Fig. 13: Example of TIR camera image in the high phase angle case.

6.3 *Optical Navigation results*

Fig. 14 shows the reconstructed trajectory for the two different sensing modalities, considering the low phase angle case study. The trajectory is correctly retrieved by both the VIS and TIR mode, however VIS images still provide the best results in terms of navigation accuracy. The localization error always tends to increase towards the end of the sequence, that is a typical feature of any SLAM algorithms, since the pose error accumulates despite BA. To quantify the navigation algorithm performances, the overall position error is computed as:

$$e_\rho = \sqrt{(x_i - \hat{x}_i)^2 + (y_i - \hat{y}_i)^2 + (z_i - \hat{z}_i)^2} \qquad [23]$$

where $\hat{x}$,$\hat{y}$,$\hat{z}$ are the position components estimates. The attitude error is instead computed following [17]:

$$e_R = arccos\left(1 - \frac{tr(\mathbf{I} - \mathbf{A}^T\hat{\mathbf{A}})}{2}\right) \qquad [24]$$

with $\hat{\mathbf{A}}$ being the estimated rotation matrix. The Root Mean Square Error (RMSE) is then reported in Table 3 for each test case scenario. As previously mentioned, since both VIS and TIR images in eclipse tend to be quite dark, the vision-based navigation algorithm cannot provide a meaningful solution. When dealing with favourable illumination conditions, i.e. low phase angle, VIS images still retain a clear advantage with respect to TIR ones, due to their wider array size. However, considering a high phase angle, VIS and TIR images lead to similar navigation performances. In the fourth case a higher thermal inertia for Ryugu's thermal model, has been assumed, which consequently led to a temperature field compatible with Hayabusa TIR capabilities even on the eclipse side. In this last scenario, VIS images are still too dark to be used for navigation purposes, while a TIR-based localization solution becomes feasible.

e

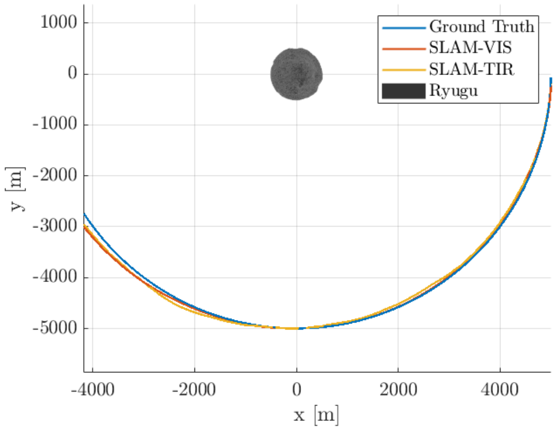

Fig. 14: SLAM results in the low phase angle case

Table 3: Localization error.

	e_ρ $[m]$	e_R $[deg]$
VIS		
Case n.1	103.08	2.45
Case n.2	236.15	11.79
Case n.3	–	–
Case n.4	–	–
TIR		
Case n.1	173.81	3.49
Case n.2	280.25	12.43
Case n.3	–	–
Case n.4	328.77	13.86

Concerning now the mapping performances of the implemented SLAM algorithm, it can be noticed that the best 3D sparse map is obtained using VIS images with a high phase angle, despite the lower navigation accuracy. The reason is that this illumination condition makes it possible to extract features that are more evenly spread on the asteroid surface, which in turn translates into a spatially uniform map. Fig. 15 shows the output 3D sparse map. Please notice that due to the selected camera FoV it was not possible to reconstruct the whole shape.

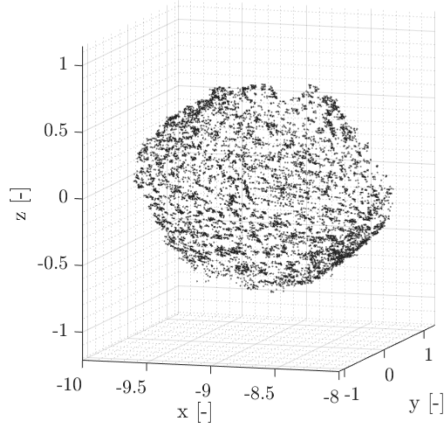

Fig. 15: 3D Sparse map

7. Conclusion

This paper studies the possibility to exploit multispectral imaging sensors for asteroids relative navigation.

A vision-based SLAM algorithm is selected as relative navigation architecture and tested with visible and thermal synthetic images. A physics-based thermal imaging generation process is proposed, starting from the asteroid thermal simulation up to the sensor response. Results show that VIS and TIR sensors contribute in different ways to navigation and are both exploitable, offering an interesting opportunity for relative navigation in close proximity of asteroids. The obtained results highlight the superiority of VIS imaging in terms of navigation accuracy, confirm the feasibility of exploiting TIR imaging for vision-based navigation. Different application scenarios in terms of illumination conditions and body temperature are critically compared.

The presented approach for relative navigation based on VIS-TIR measurements is tested for an asteroid target, but it represents a promising option for a wide set of applications, including other types of targets. Future work will include the refinement of the thermal model and the assessment of image-fusion algorithms for improving the navigation performance.

References

[1] Shape models, their derivatives, and relating data and tools of the asteroid Ryugu by Watanabe et al. (2019). https://data.darts.isas.jaxa.jp/pub/hayabusa2/paper/Watanabe_2019/README.html. Last accessed: July 2021.

[2] The ultimate infrared handbook for R&D professionals. https://www.flirmedia.com/MMC/THG/Brochures/T559243/T559243_EN.pdf. Last accessed: July 2021.

[3] Oleksandr Bailo, Francois Rameau, Kyungdon Joo, Jinsun Park, Oleksandr Bogdan, and In So Kweon. Efficient adaptive non-maximal suppression algorithms for homogeneous spatial keypoint distribution. *Pattern Recognition Letters*, 106:53 – 60, 2018.

[4] Axel Beauvisage, Nabil Aouf, and Hugo Courtois. Multi-spectral visual odometry for unmanned air vehicles. In *2016 IEEE International Conference on Systems, Man, and Cybernetics (SMC)*, pages 001994–001999. IEEE, 2016.

[5] Paulo Vinicius Koerich Borges and Stephen Vidas. Practical infrared visual odometry. *IEEE Transactions on Intelligent Transportation Systems*, 17(8):2205–2213, 2016.

[6] Jean-Yves Bouguet et al. Pyramidal implementation of the affine lucas kanade feature tracker description of the algorithm. *Intel corporation*, 5(1-10):4, 2001.

[7] E Brageot, O Groussin, P Lamy, and J-L Reynaud. Experimental study of an uncooled microbolometer array for thermal mapping and spectroscopy of asteroids. *Experimental Astronomy*, 38(3):381–400, 2014.

[8] Long Chen, Libo Sun, Teng Yang, Lei Fan, Kai Huang, and Zhe Xuanyuan. Rgb-t slam: A flexible slam framework by combining appearance and thermal information. In *2017 IEEE International Conference on Robotics and Automation (ICRA)*, pages 5682–5687. IEEE, 2017.

[9] Alan M. Didion, Austin K. Nicholas, Joseph E. Riedel, Robert J. Haw, and Ryan C. Woolley. Methods for Passive Optical Detection and Relative Navigation for Rendezvous with a Non-Cooperative Object at Mars. In *AAS/AIAA Astrodynamics Specialist Conference*, Snowbird, UT, 2018.

[10] Rikke Gade and Thomas B Moeslund. Thermal cameras and applications: a survey. *Machine vision and applications*, 25(1):245–262, 2014.

[11] Olivier Groussin, Nicholas Attree, Yann Brouet, Valérie Ciarletti, Björn Davidsson, Gianrico Filacchione, H-H Fischer, Bastian Gundlach, Martin Knapmeyer, Jörg Knollenberg, et al. The thermal, mechanical, structural, and dielectric properties of cometary nuclei after rosetta. *Space Science Reviews*, 215(4):1–51, 2019.

[12] Anup Bharat Katake. *Modeling, image processing and attitude estimation of high speed star sensors*. PhD thesis, Texas A&M University, 2006.

[13] K Kitazato, RE Milliken, Takahiro Iwata, Masanao Abe, Makiko Ohtake, S Matsuura, T Arai, Yusuke Nakauchi, T Nakamura, Moe Matsuoka, et al. The surface composition of asteroid 162173 ryugu from hayabusa2 near-infrared spectroscopy. *Science*, 364(6437):272–275, 2019.

[14] Vincent Lepetit, Francesc Moreno-Noguer, and Pascal Fua. Epnp: An accurate o(n) solution to the pnp problem. *International Journal Of Computer Vision*, 81:155–166, 2009.

[15] Jiayi Ma, Yong Ma, and Chang Li. Infrared and visible image fusion methods and applications: A survey. *Information Fusion*, 45:153–178, 2019.

[16] Marina Magnabosco and Toby P Breckon. Cross-spectral visual simultaneous localization and mapping (slam) with sensor handover. *Robotics and Autonomous Systems*, 61(2):195–208, 2013.

[17] Landis Markley and D. Mortari. Quaternion attitude estimation using vector observations. *Journal of the Astronautical Sciences*, 48, 04 2000.

[18] D. Nister. An efficient solution to the five-point relative pose problem. *IEEE Transactions on Pattern Analysis and Machine Intelligence*, 26(6):756–770, 2004.

[19] Tatsuaki Okada. Thermography of asteroid and future applications in space missions. *Applied Sciences*, 10(6):2158, 2020.

[20] Tatsuaki Okada, Tetsuya Fukuhara, Satoshi Tanaka, Makoto Taguchi, Takeshi Imamura, Takehiko Arai, Hiroki Senshu, Yoshiko Ogawa, Hirohide Demura, Kohei Kitazato, et al. Thermal infrared imaging experiments of c-type asteroid 162173 ryugu on hayabusa2. *Space Science Reviews*, 208(1):255–286, 2017.

[21] E. Rublee, V. Rabaud, K. Konolige, and G. Bradski. Orb: An efficient alternative to sift or surf. In *2011 International Conference on Computer Vision*, pages 2564–2571, 2011.

[22] Yuri Shimaki, Hiroki Senshu, Naoya Sakatani, Tatsuaki Okada, Tetsuya Fukuhara, Satoshi Tanaka, Makoto Taguchi, et al. Thermophysical properties of the surface of asteroid 162173 ryugu: Infrared observations and thermal inertia mapping. *Icarus*, 348:113835, 2020.

[23] P.H.S. Torr and A. Zisserman. Mlesac: A new robust estimator with application to estimating image geometry. *Computer Vision and Image Understanding*, 78(1):138 – 156, 2000.

[24] Xiao-Shan Gao, Xiao-Rong Hou, Jianliang Tang, and Hang-Fei Cheng. Complete solution classification for the perspective-three-point problem. *IEEE Transactions on Pattern Analysis and Machine Intelligence*, 25(8):930–943, 2003.